REVIEW

Check for updates

Single-atom catalysts for thermal- and electro-catalytic hydrogenation reactions

Jingfang Zhang,[a] Hongjuan Zhang,[a] Yongmeng Wu,[b] Cuibo Liu,[b] Yi Huang, [ID] *[bc] Wei Zhou [ID] *[b] and Bin Zhang [ID] *[b]

Hydrogenation reactions are among the most significant transformations in the chemical, energy, and environmental industries, which calls for a new generation of promising catalysts towards economic growth and environmental sustainability. Single-atom catalysts (SACs) have emerged as attractive candidates because of their maximum atom utilization, and high catalytic activity and selectivity. In this review, we introduce the unique properties of SACs including structural and electronic features, to guide the rational design of SACs and demonstrate a more detailed understanding of reaction mechanisms. Then, thermal catalytic hydrogenation of organic compounds and electrocatalytic hydrogenation with a particular focus on nitrate electroreduction reactions over SACs are further summarized, and the underlying mechanisms are discussed. Finally, the emerging issues and related perspectives for the future development of SACs in this field are proposed.

1. Introduction

Hydrogenation is one of the most important transformations used for manufacture and processing in the petrochemical, fine chemical, and environmental industries.[1–5] Generally, the hydrogenation reaction refers to a reduction process, which results in the addition of hydrogen to unsaturated compounds. The compounds are not only limited to organic ones (such as alkynes, aldehydes, alkenes, ketones, nitroarenes, and so on), but also span a variety of inorganic ones (such as metal carbonates, nitrates, carbon dioxide, nitrogen, and so on).[6–10] The thermal-catalytic hydrogenation reaction, in most cases, uses gaseous hydrogen (H_2) as the hydrogen source to reduce unsaturated compounds with a suitable catalyst capable of dissociating hydrogen gas. For example, in the thermal-catalytic hydrogenation of alkynes under reaction conditions of 175 °C and 0.1 MPa H_2, ethylene could be obtained at 94% conversion over the Au/SiO_2 catalyst.[11] However, hydrogenation by thermal catalysis is impractical when H_2 is unavailable. Alternatively, electricity can be stored to supply reduction equivalents,[12] and thus the electrochemical method is emerging as a promising approach for hydrogenation transformations. In hydrogenation reactions including both thermal- and electro-catalytic transformations, selectivity holds the key to the production of desired products. Selective hydrogenation reactions provide

a great opportunity for improving the selectivity, which means that one of the functional groups is preferentially hydrogenated to a certain degree while others remain intact, when two or more unsaturated functional groups are present in one substrate, or different unsaturated substrates exist in the catalytic system.[13] For example, unsaturated hydrocarbons such as alkynes and alkenes coexist in the raw materials of the petroleum industry, and it is expected that alkynes are selectively hydrogenated to alkenes while alkenes either produced or fed are not further saturated to alkanes. Therefore, selective hydrogenation transformations are of great importance for the efficient production of targeted chemicals in both bulk and fine chemical industries.

The achievement of selective hydrogenation transformations is largely attributed to highly active and selective catalysts. Currently, catalysts can be classified as homogeneous and heterogeneous catalysts with metal centers as active sites. Homogeneous catalysts often exhibit high selectivity because of their well-defined single-site structure, however, the disadvantages of poor stability, hard separation, and difficulty to reuse make them unfavorable for industrial applications.[14] In contrast, heterogeneous catalysts dominate large-scale industrial production in terms of reusability, easy separation, and good stability even under relatively harsh reaction conditions. The selectivity of heterogeneous catalysts in hydrogenation reactions relies on the absorption ability of reaction intermediates on the surface of catalysts, which is determined by the electronic and geometric structures of active sites.[15] Multiple catalytic sites in common heterogeneous catalysts possess different coordination environments and electronic structures, leading to various adsorption modes of reaction intermediates

[a]Department of Chemistry, College of Science, Hebei Agricultural University, Baoding 071001, China

[b]School of Science, Institute of Molecular Plus, Tianjin University, Tianjin 300072, China. E-mail: weizhou@tju.edu.cn; bzhang@tju.edu.cn

[c]Institute of Environmental & Applied Chemistry, College of Chemistry, Central China Normal University, Wuhan 430079, China. E-mail: yihuang@mail.ccnu.edu.cn

and thus poor selectivity. Taking the semi-hydrogenation of acetylene over the Pd metal surface as an example, three possible adsorption modes of ethylene may occur in the reaction process according to the configuration of Pd atoms: ethylidyne mode and di–σ mode on continuous Pd active sites (3-fold sites and 2-fold sites, respectively), and π-bonded mode on isolated Pd single atoms.[16,17] The strong absorption strength of ethylidyne mode or di–σ mode will result in dimerization or over-hydrogenation of acetylene into ethane, and the weak absorption strength of π-bonded mode is conducive to the desorption of ethylene from the Pd surface and thus prevents its further hydrogenation to ethane.[18,19] Therefore, it is highly desirable to construct heterogeneous catalysts with well-defined and uniform active sites for achieving excellent selectivity in hydrogenation transformations.

Single-atom catalysts (SACs) with atomically dispersed metal atoms on supports have recently emerged as a new frontier to bridge the gap between homogeneous catalysts with well-defined structures and heterogeneous catalysts with structural varieties. The ultimate dispersion of SACs typically relies on strong interactions between single atoms and supports, where supports can be considered to serve the role of ligands in homogeneous catalysts.[20] In turn, the strong interactions in SACs will afford them a unique electronic structure and coordination environment, which are directly related to their catalytic activity in thermal- and electro-catalytic reactions, including selective hydrogenation transformations.[15,20–24] Moreover, the homogeneity of active sites in SACs provides great potential to achieve a high selectivity because of their uniform electronic and geometric structures. The well-defined and uniform structures of SACs provide a promising platform to study relationships between the structure and catalytic performance, and facilitate a comprehensive understanding of the reaction mechanism, achieving a rational design principle for SACs.

In this review, we summarize recent advances in SACs towards hydrogenation reactions *via* thermal- and electro-catalytic transformations. The unique geometric and electronic structures of SACs and the general design principle for constructing high-performance SACs are summarized. Then, we focus on their applications in hydrogenation reactions including thermal-catalytic hydrogenation of organic compounds and electro-catalytic nitrate reduction reactions, with an attempt to reveal the potential influencing factors on catalytic activity and selectivity and illustrate the underlying mechanisms at the molecular level. Lastly, the major challenges and opportunities for future research on the design of SACs for hydrogenation reactions are presented.

2. Unique properties and design principles of SACs

Supported metals are among the most important catalysts in many critical applications, for example, chemical transformation, energy conversion, and environmental remediation. In fact, a large proportion of metal atoms are not involved in the

catalytic reaction, because catalysis mainly occurs on the surface of catalysts. Hence, smaller sized metals with high surface/volume ratios will possess more catalytically active sites, in favor of the promotion of catalytic performance. When the size of the metal is decreased from bulk to single atoms, its geometric and electronic structures will strongly change (Fig. 1). The size effects can be mainly featured in the following aspects: (1) More atoms with an unsaturated coordination environment are exposed on the surface.[25,26] (2) Due to the quantum size effect, the confinement of electrons will lead to the shift from continuous energy bands to discrete atomic orbitals, increased energy levels and a distinctive highest occupied molecular orbital (HOMO) – lowest unoccupied molecular orbital (LUMO) gap.[27–29] (3) The chemical bonding of metal and the support becomes stronger and charge transfer may occur between them.[30,31] As a result, these size-dependent effects will cause distinct reactivities in bulk and counterparts.

SACs with isolated metal single atoms on the support represent a new generation of catalysts owing to their dual advantages of homogeneous and heterogeneous catalysis. With maximum atom utilization, the development of SACs provides a promising approach to reasonable use of metal resources and achieving atomic economy, especially for noble-metal-based catalysts.[32–36] In terms of reactivity, SACs with fully exposed atoms possess more active sites, and the unsaturated coordination environment and charge transfer between single metal atoms and the support will effectively improve the intrinsic activity of active sites.[37,38] In this regard, a variety of synthetic methodologies have been developed for SACs. For example, mass-selected soft loading[39] and atomic layer deposition[40,41] are powerful methods to synthesize SACs. However, the two methods are not suitable for large-scale production due to the requirement of expensive equipment and low yield. Currently, wet-chemistry methods for fabricating SACs, such as defect engineering strategy,[42–44] spatial confinement strategy[45–47] and coordination design strategy,[48–50] have been widely implemented. Moreover, advanced characterization techniques have provided powerful support to confirm the structures of SACs.
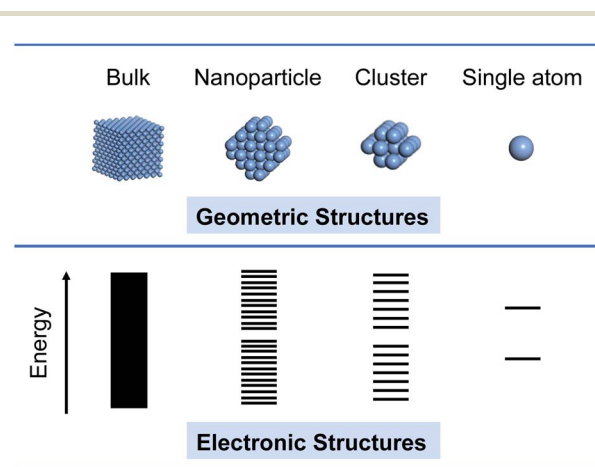

Fig. 1 Geometric and electronic structures of bulk, nanoparticles, clusters, and single atoms.

Scanning tunneling microscopy (STM) and aberration-corrected electron microscopy (ACEM) techniques can offer direct routes to observe single atoms.[51,52] Synchrotron-radiated X-ray absorption fine structure (XAFS) can provide average information about the local atomic and electronic structure of single atoms and their neighboring atoms.[53,54] Using CO as the probe molecule, Fourier transform infrared (FTIR) spectroscopy can provide additional information to determine the structure and dispersion of metal centers.[55,56] By combining these characterization techniques with density functional theory (DFT) calculations, great progress will be made in design and synthesis, expansion of application fields, and further uncovering the activity origin of SACs.

Heterogeneous catalysis usually involves the adsorption of reactants on a catalyst, the surface reaction of adsorbed species, and the desorption of products.[57] Generally, the initial absorption behavior determines the following reaction pathways, and is correlated with the catalytic activity and selectivity.[58] In terms of the absorption behavior, the absorption manner and strength of a reactant in SACs are totally different from those in metal nanoparticles/clusters. Due to the atomic and homogeneous dispersion of metal atoms in SACs, the only absorption mode of the substrate atop the metal site is allowed, leading to excellent catalytic selectivity. In contrast, supported metal nanoparticles/clusters with continuous assemblies of metal atoms usually have multiple absorption modes with the tendency of 3-fold sites, followed by 2-fold and atop sites,[16,17] and consequently the catalytic selectivity is poor. Because of the ultimate dispersion of active metals in SACs, the single metal atom is directly bonded to the functional species on the support and stabilized by the interactions between single metal atoms and the support. The unsaturated coordination configuration and the unique electronic structure of metal sites provided by the metal-support interactions in SACs are usually considered to be responsible for the optimized adsorption strength of the reactant and thus the extraordinary catalytic activity. For example, Zhang and co-workers synthesized Ru/NC SACs by pyrolysis of ruthenium acetylacetonate and C, N-containing precursors for the reductive amination of aldehydes/ketones.[59] When the pyrolysis temperature is changed, both the Ru–N coordination structure (e.g., $Ru_1–N_5$, $Ru_1–N_4$, and $Ru_1–N_3$) and the electron density of the Ru single atoms are varied, leading to different catalytic performance. As a consequence, the resulting $Ru_1–N_3$ structure with the largest electron density exhibits moderate capability for hydrogen activation, which affords the highest activity and selectivity for the reductive amination of aldehydes/ketones to primary amines. In general, regulating the geometric and electronic structures of active metal centers *via* metal-support interactions can be exploited as a common design principle for more efficient SACs towards specific reaction pathways.[20,60,61]

3. Thermal- and electro-catalytic hydrogenation reactions over SACs

3.1 Thermal-catalytic hydrogenation reactions

3.1.1 Activation pathway of H_2.
In thermal-catalytic hydrogenation transformations, H_2 is an indispensable feed
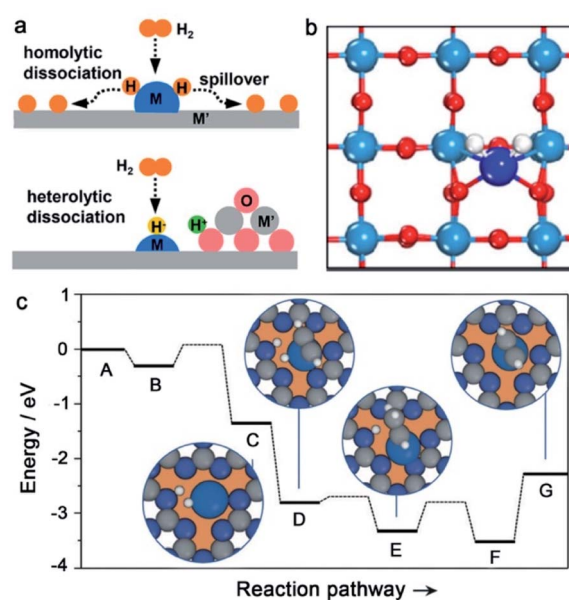

Fig. 2 (a) Two representative H_2 activation pathways: homolytic and heterolytic dissociation of H_2. Reproduced with permission from ref. 15. Copyright 2021 American Chemical Society. (b) Adsorption of H_2 on Pt/WO_x(001) SACs. Reproduced with permission from ref. 65. Copyright 2020 Elsevier. (c) Energies and models for Pd SAC catalyzed hydrogenation of acetylene. Reproduced with permission from ref. 67. Copyright 2015 John Wiley and Sons.

gas. The step of H_2 activation (e.g., dissociation manner) is vital for the selectivity of hydrogenation reactions. Generally, the dissociation behavior of H_2 can be classified as homolysis and heterolysis (Fig. 2a).[13,15]

In the homolytic pathway, H_2 is homolytically dissociated into H atoms to form two metal–$H^{\delta-}$ species. The homolytic dissociation of H_2 always occurs on the metal surface with partially occupied d-orbitals (such as VIII group metals), which can accept the σ electrons of H_2 and donate d-electrons to the σ* antibonding orbital of H_2. Due to the donation behavior of d-electrons, it is more favorable for metal sites with a high electron density to proceed with the homolytic dissociation of H_2. Moreover, the completion of the homolytic dissociation of H_2 often requires multi-center ensembles of metal surfaces in a heterogeneous metal catalyst. Although the two hydrogen species formed in a homolytic pathway have indistinguishable reactivities, hydrogen spillover occurs easily on metal surfaces, for example, hydrogen species migrate from the metal surface to the support, accompanied by the electron transfer process and simultaneous reduction of the support surface.[13] In this way, the H_2 activation and hydrogenation sites are physically separated. When the operation conditions change (e.g., hydrogen partial pressure), hydrogen reverse spillover can also happen, which is thermodynamically favorable for late transition metals, except for Au.[62–64] Interestingly, SACs (e.g., Pt_1/WO_x) have recently been reported to cleave H_2 in a homolytic dissociation pathway (Fig. 2b).[65] The Pt single atoms are well stabilized by the oxygen vacancies on the WO_x(001) surface. Due to the electron transfer from oxygen vacancies to the Pt single

This journal is © The Royal Society of Chemistry 2022

J. Mater. Chem. A, 2022, **10**, 5743–5757 | **5745**

atoms, Pt single atoms carry a negative charge. The DFT results prove that the negatively charged Pt single atoms can facilitate the homolytic dissociation of H_2 to metal–$H^{\delta-}$ species, resembling that occurring in metal ensembles. However, the as-formed metal–H species prefer to transfer to its neighboring O_{2c} on WO_x, implying a hydrogen spillover process to form Brønsted acid sites. As a result, the H_2 dissociation on the Pt_1/WO_x surface occurs in a heterolytic pathway, but it involves a combination of the homolytic cleavage and the further hydrogen spillover process.

In the heterolytic pathway, H_2 is heterolytically dissociated into H^+/H^- pairs. Different from the homolytic dissociation pathway, H_2 molecules can be readily dissociated on electron-deficient metal sites in a heterolytic manner. The heterolytic dissociation of H_2 often requires the assistance of nucleophilic atoms from supports or surface organic modifiers, where H^+ binds to a proton acceptor (*e.g.*, O or N atom) and H^- binds to a d-block metal atom.[66] The produced H^+/H^- pairs prefer to reduce polar unsaturated groups, which can largely improve the selectivity of hydrogenation reactions. When the polar unsaturated groups are far away from metal sites, they can also be hydrogenated in the outer sphere because the H^+/H^- pairs can migrate from the catalyst to the substrates. The heterolytic activation pathway is well known in both homogeneous and heterogeneous catalysts. SACs as a new generation of catalysts have also been reported to activate H_2 by the heterolytic pathway. For example, Pérez-Ramírez and co-workers synthesized Pd SACs by anchoring Pd atoms into the cavities of mesoporous polymeric graphitic carbon nitride (mpg-C_3N_4).[67] The activation of H_2 takes place through the heterolytic dissociation pathway on single-site Pd, where the cleaved H^+ moves to a nearby N atom from mpg-C_3N_4 to yield N–$H^{\delta+}$, and the cleaved H^- binds to the Pd atom to form Pd–$H^{\delta-}$. The step is almost barrier-free and exothermic by -1.34 eV compared with the zero-point energy of the gas-phase molecule. The favorable H_2 activation step is beneficial to the following hydrogenation process. DFT calculations prove that the hydrogenation of acetylene is a stepwise process (Fig. 2c), which begins with $H^{\delta-}$ transfer from Pd to absorbed acetylene on the Pd site, and then $H^{\delta+}$ from a nearby N–H group adds to the half-hydrogenated intermediate generated in the previous step. Following this pathway, the hydrogenated products (*i.e.*, alkenes) are obtained.

3.1.2 Mechanisms of thermal-catalytic hydrogenation on SACs. Traditional heterogeneous catalysts for thermal-catalytic hydrogenation reactions are either bulk or nanoparticles (>2 nm size), where a substantial portion of the inner metal atoms are hidden by the surface ones and cannot be utilized to play their active roles. Moreover, these catalysts usually exhibit a wide variety in size, composition, and structure, which leads to various absorption modes for reaction intermediates and thus poor chemoselectivity. With the growing demand for active, selective, and low-cost catalysts, SACs for thermal-catalytic hydrogenation reactions have attracted much attention due to their highly exposed active sites, structural uniformity, and maximized atom efficiency. With the rapid development of advanced characterization techniques and theoretical calculations, SACs provide an ideal platform to

investigate the reaction mechanisms because of their advantages of structural simplicity and homogeneity. In this section, we mainly describe recent experimental and computational advances in thermal-catalytic hydrogenation reactions over SACs to gain insights into the single atom and its surrounding environment at the molecular level and obtain a comprehensive understanding of structure–performance relationships.

3.1.2.1 Support effect. It has been well established that the H_2 activation step is highly related to the geometric and electronic structures of catalytic metal centers.[68] As for SACs, the single atoms are stabilized by the strong interactions with the support *via* metal–metal bonds or coordination with heteroatoms (*e.g.*, O, S, N, *etc.*) in the support, which can, in turn, regulate the local chemical environment of catalytic metal sites. In this regard, the underlying supports play a critical role in determining the performance of SACs in thermal-catalytic hydrogenation transformations. Many important types of supports have been developed, such as metals,[69] metal (oxyhydr) oxides,[70–72] carbides,[73] zeolites,[74] carbon-based nanomaterials,[75] *etc.*

In SACs, most attention is paid to the binding sites with metal centers in the first coordination sphere (Fig. 3), analogous to the ligands of metalloenzymes in nature. The nature of binding sites provides a great possibility for the modulation of the electronic structure of metal centers and thus the catalytic performance. For example, Li and co-workers employed a template-sacrificial approach to construct Fe single atoms on P-doped carbon for hydrogenation of different unsaturated compounds (*e.g.*, N-heterocycles, and functionalized nitroarenes).[76] Their experimental and theoretical results proved that one Fe single atom was coordinated with four P atoms and one dioxygen molecule, forming a pyramidal O_2–Fe–P_4 structure. The O_2–Fe–P_4 sites can be reduced by H_2 to transform into Fe–P_4 sites during hydrogenation catalysis, which exhibited high activity and selectivity. However, the corresponding Fe–N–C catalyst with planar Fe–N_4 active sites was almost inactive for these hydrogenation reactions under the same reaction

Fig. 3 Schematic of the first and second coordination spheres in SACs. Reproduced from ref. 68, under terms of Creative Commons license, published 2018 Oxford University Press.

conditions. The comparison of Fe–P$_4$ sites and Fe–N$_4$ sites in hydrogenation performance suggested the important role of P binding sites with Fe single atoms for the hydrogenation activity.

When the binding atoms with metal centers remain the same, altering the type of binding species can also tune the catalytic hydrogenation performance. Li and co-workers synthesized a series of Cu single atoms on N-doped carbon and investigated the influence of N-doping types (pyrrolic-N and pyridinic-N) on catalytic hydrogenation performance of quinoline (Fig. 4a and b).[75] The dominant pyrrolic-N in Cu SACs displayed two fold improved activity compared to pyridinic-N doped Cu SACs. Differential charge density analysis revealed that the electron density of Cu species with pyrrolic-N coordination was higher than that with pyridinic-N coordination, which was beneficial for the formation of the Cu–H bond and decreased the energy barrier of the hydrogenation pathway, thus leading to the enhanced hydrogenation performance. Similarly, the type of P species coordinated with catalytic metal centers also affects the hydrogenation activity.[76] A series of single-atom Fe on P-doped carbon with different percentages of graphitic P group (P$_{grap}$) were prepared by changing the carbonization temperature (denoted as Fe–P$_x$–PCCs, where x stands for the carbonization temperature). It was found that the content of P$_{grap}$ was highly correlated with the conversion of quinoline catalyzed by Fe–P$_x$–PCCs (Fig. 4c). As a result, the Fe–

P$_{900}$–PCC catalyst with the highest P$_{grap}$ content exhibited the best hydrogenation activity.

In addition, changing the coordination number (CN) of metal centers, even with the same binding atom, often has an effect on thermal-catalytic hydrogenation performance. For example, Zhang and co-workers used ethanediamine to chelate Pt cations and then removed the ligand by rapid thermal treatment (RTT) to prepare Pt single atoms on the Fe$_2$O$_3$ support (Pt$_1$/Fe$_2$O$_3$-T, T stands for the RTT temperature), which acted as the model catalyst to investigate the relationships between the coordination structure of the Pt single atom and hydrogenation activity.[72] The CN of Pt–O and oxidation state of Pt can be finely tuned by adjusting the RTT temperature. As the RTT temperature increased from 500 to 600 °C, the CN of Pt–O in the first shell continuously decreased from 3.8 to 1.8, and the oxidation state of Pt became lower (Fig. 4d). Correspondingly, Pt$_1$/Fe$_2$O$_3$-600 exhibited the best activity with the highest turnover frequency (TOF) of 3809 h^{-1} at 40 °C among all the Pt$_1$/Fe$_2$O$_3$-T catalysts. As a result, the hydrogenation activity can be well optimized by modifying the coordination and electronic structures of the Pt single atoms. DFT calculations proved that H$_2$ can dissociate spontaneously on two-coordinated Pt$_1$/Fe$_2$O$_3$-600, while three-coordinated Pt$_1$/Fe$_2$O$_3$-550 and four-coordinated Pt$_1$/Fe$_2$O$_3$-500 need a barrier of 0.25 and 0.91 eV to dissociate H$_2$, respectively (Fig. 4e). It can be concluded that the lower the Pt–O CN, the easier the H$_2$ dissociation on Pt SACs, thus the higher the hydrogenation activity of Pt SACs. Such a structure–performance relationship with CN as a key descriptor is also established in SACs for various catalytic applications, such as Fe SACs for selective oxidation of the C–H bond,[77] and Co SACs for CO$_2$ electroreduction.[78]

Beyond the first coordination sphere, the metal cations in metal-based supports, or the functional groups of the carbon substrate (*e.g.*, epoxy groups) in the second coordination sphere (Fig. 3) are readily involved in the catalytic process,[79,80] and also have an important effect on hydrogenation performance. For example, Gates and co-workers studied the catalytic performance of ethene hydrogenation over supported single-site Ir complexes (Ir(C$_2$H$_4$)$_2$(acac)).[79] MgO and HY zeolite (DAY zeolite) were employed as the supports. The rational design of the two supported catalysts ensured the uniformity in the first coordination sphere, where each Ir atom was coordinated with two oxygen atoms from MgO or DAY zeolite supports and two C$_2$H$_4$ ligands. By evaluating the ethene hydrogenation activity, they found that the Ir complexes on DAY zeolite exhibited 20 times activity enhancement compared to that on MgO. Because of the electron-withdrawing effect of DAY zeolite, the electron density of Ir on DAY zeolite was much lower than that on MgO. The deficient electron structure of Ir on DAY zeolite allowed the simultaneous bonding of Ir with both H$_2$ and C$_2$H$_4$, facilitating the hydrogenation process. In contrast, the electron enrichment of Ir on MgO suppressed the above bonding process, thus hindering the step of H$_2$ activation and leading to a poor catalytic activity. The engineering of the second coordination sphere to optimize the catalytic performance was also demonstrated in electrocatalysis, such as the NiFe coordination polymer catalyst
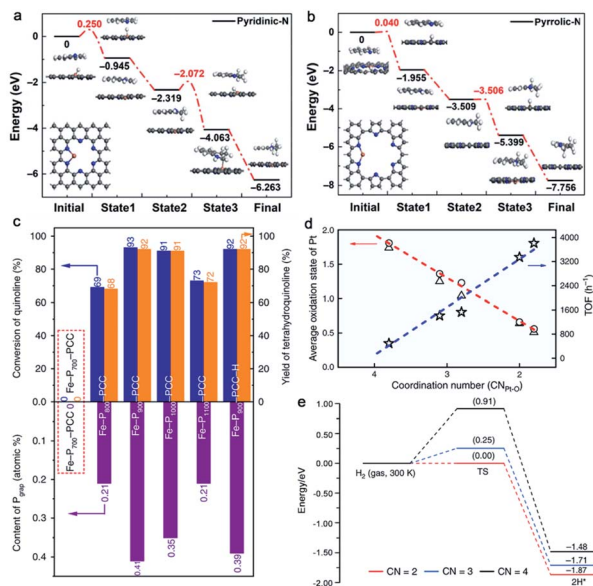

Fig. 4 Quinoline hydrogenation process for the coordination of pyridinic-N (a) and pyrrolic-N (b). Reproduced from ref. 75, under the terms of Creative Commons license, published 2020 Springer Nature. (c) The relationships between hydrogenation activity of quinoline and the content of P$_{grap}$. Reproduced from ref. 76, under the terms of Creative Commons license, published 2020 Springer Nature. (d) The correlation between the coordination number of Pt–O and the average oxidation state of Pt and hydrogenation activity of Pt SACs. (e) Energy barriers of H$_2$ dissociation on Pt SACs with different coordination numbers of Pt–O. Reproduced from ref. 72, under the terms of Creative Commons license, published 2019 Springer Nature.

This journal is © The Royal Society of Chemistry 2022

J. Mater. Chem. A, 2022, **10**, 5743–5757 | **5747**

for water oxidation[81] and Co SACs for acidic oxygen reduction reaction.[80]

In addition, the CN of metal centers in the first coordination sphere can be tuned by regulating the second coordination sphere, which is often accompanied by different catalytic performances. For example, Zheng and co-workers employed various supports (*e.g.*, Cu_2O, Al_2O_3, ZnO, and TiO_2) to anchor atomically dispersed Pd catalysts for semihydrogenation of terminal alkynes.[71] They demonstrated that atomically dispersed Pd on the Cu_2O (Pd_1/Cu_2O) catalyst exhibited high activity and selectivity in the hydrogenation of alkynes, while Pd on other supports was inactive. The Pd_1/Cu_2O catalyst was prepared by the galvanic displacement reaction between Pd^{2+} and Cu^+ of the Cu_2O support. The high-angle annular dark-field scanning transmission electron microscopy (HAADF-STEM) image showed the atomic distribution of Pd (Fig. 5a). Extended X-ray absorption fine structure (EXAFS) spectroscopy revealed the existence of Pd–O and Pd–Cu bonds without the Pd–Pd bond in the Pd_1/Cu_2O catalyst (Fig. 5b). X-ray absorption near-edge structure (XANES) spectra were used to analyze the valence state of Pd (Fig. 5c). The valence of Pd in Pd_1/Cu_2O is +1 and two-coordinated, while Pd on other metal oxide supports is close to +2 and is four-coordinated. The lower valence and unsaturated coordination structure of Pd in Pd_1/Cu_2O favor the heterolytic activation pathway of H_2 to yield $O–H^{\delta+}$ and $Pd–H^{\delta-}$ species. DFT calculations confirm that the activation barrier was 0.33 eV, and the reaction energy was exothermic by 0.79 eV (Fig. 5d). In contrast, the valence state of +2 and the four-coordinated structure of Pd on other metal oxide supports make Pd inactive for H_2 activation, leading to poor catalytic activities. Moreover, the desorption energy (0.26 eV) of styrene on H_2-preadsorbed Pd(I) on Pd_1/Cu_2O is higher than the energy barriers (0.32 and 1.26 eV) required for the following addition of H atoms onto styrene, which effectively prevents the over-hydrogenation of phenylacetylene and thus promotes the selectivity (Fig. 5e). More importantly, Pd_1/Cu_2O also exhibits wide applicability in the hydrogenation of many alkynes with high selectivity. This work provides a good demonstration of the tunability of activity and selectivity in hydrogenation catalysis by manipulating the local coordination environment of active sites *via* the second coordination sphere.

Therefore, it is important to understand the structure–performance relationships of SACs at the molecular level, including the first and second coordination spheres, rather than individual metal centers.

3.1.2.2 The effect of dopants. In heterogeneous catalysis, it is well known that doping is an effective way to tune the electronic structure of catalytic metal centers and modify the adsorption behavior of reactants, achieving the optimized catalytic performance. Introducing dopants into the vicinal metal sites in SACs can also make a significant influence on catalytic reactivity.

The Group I alkali metals (*e.g.*, Li, Na, and K) lie in the s-block of the periodic table, which readily donate the single s electron in their valence shell. Since the first discovery of the alkali doping effect in 1845,[82] the roles of alkali additives have been extensively studied in thermal-catalytic hydrogenation reactions.[83,84] Recently, the addition of alkali metal cations into
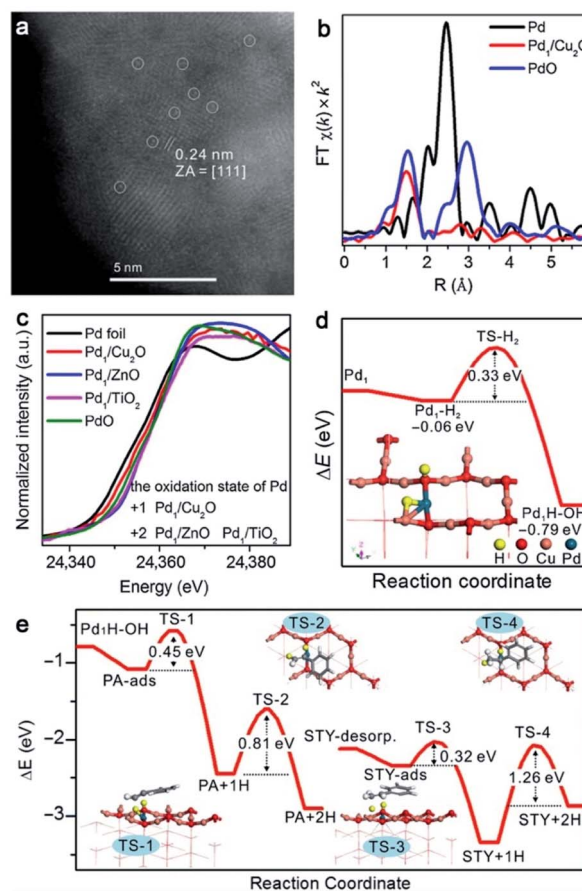

Fig. 5 (a) HAADF-STEM image of Pd_1/Cu_2O. (b) EXAFS spectra at the Pd K-edge of Pd_1/Cu_2O, Pd foil, and PdO. (c) XANES spectra of Pd catalysts on various supports, Pd foil, and PdO. (d) Energies and model of Pd_1/Cu_2O in the heterolytic activation of H_2. (e) Energies of intermediates and transition states for hydrogenation of phenylacetylene on Pd_1/Cu_2O. Reproduced from ref. 71, published in CCS Chemistry 2019; Cu_2O-supported atomically dispersed Pd catalysts for semi-hydrogenation of terminal alkynes: critical role of oxide supports is available online (DOI: 10.31635/ccschem.019.20190008).

SACs has been reported to promote the hydrogenation reactions *via* electronic and structural effects.[85–87] Another important role of alkali metal cations is that they are able to stabilize the single metal atoms to prevent their aggregation in the presence of hydrogen.[88–90] Taking the Pt SAC (with a Pt loading amount of 2.16%) catalyzed hydrogenation reaction of 3-nitrostyrene as an example, the obtained 3-aminostyrene in a high yield relies on the high chemoselectivity of the hydrogenation reaction. According to the previous reports, it is hard to achieve high selectivity over high-loading Pt catalysts due to the easy aggregation properties of single atoms to nanoparticles (with a diameter >1 nm) with high loadings.[91] Zhang and co-workers reported that it is possible to transform the nonchemoselective high loading Pt/FeO_x catalyst into a highly chemoselective one by the addition of the alkali metal (Fig. 6a).[92] By addition of 5 wt% Na, the resulting 5% Na to 2.16% Pt/FeO_x catalyst exhibited the best catalytic performance for the hydrogenation reaction of 3-nitrostyrene, with an enhanced chemoselectivity of

97.4% to 3-aminostyrene compared to that of 66.4% for the Na-free 2.16% Pt/FeO$_x$ catalyst. At the same time, no obvious change was observed in the catalytic activity of 5% Na to 2.16% Pt/FeO$_x$ and Na-free 2.16% Pt/FeO$_x$ catalysts. As shown in Fig. 6b and c, it seems that the average size of Pt particles increases after the introduction of Na ions. However, by examination of an individual Pt particle (Fig. 6d and e), one can see that the particles in the 5.03% Na to 2.16% Pt/FeO$_x$ catalyst are assembled by loosely and randomly stacked single atoms or clusters of only a few atoms, in contrast with the well-crystallized Pt particles in the 2.16% Pt/FeO$_x$ catalyst. In other words, the Na cations can serve the role of 'interfacial chemical glue' to stabilize the single Pt atoms and restrain the formation of the Pt nanocrystal. The XANES results of the Pt L$_{III}$ edge displayed a gradual increase in the whiteline intensity with an increased Na content in these catalysts, indicating that the oxidation state of Pt became more positive. They attributed the positively charged Pt to the interactions between Pt and surface NaFeO$_2$ species via a bridge linkage of Pt–O–Na–O–Fe. Further characterization indicated that the nitro group was more preferentially and strongly adsorbed on NaFeO$_2$ compared with FeO$_x$, leading to the high chemoselectivity of the nitro group hydrogenation over the 5.03% Na to 2.16% Pt/FeO$_x$ catalyst.

Zheng and co-workers also demonstrated the promotion effect of alkali cations in the hydrogenation of various substrates.[93] They fabricated two Ru SACs on Al$_2$O$_3$ using NaOH and NH$_4$OH as precipitators, denoted as Ru(Na) and Ru(H), respectively. Ru(Na) exhibited enhanced activity and stability in the hydrogenation catalysis compared with those of Ru(H),

which can be explained by two important functions of Na$^+$ cations. On one hand, H$_2$ can be favorably dissociated in a heterolytic manner to form Ru–H$^{\delta-}$ and O–H$^{\delta+}$. The presence of Na$^+$ cations can stabilize hydride species owing to the stronger Na$^+\cdots$H$^{\delta-}$ attraction on Ru(Na) than H$^+\cdots$H$^{\delta-}$ attraction on Ru(H). Furthermore, the coulombic interactions also restrain the hydride species over Ru(III) from migrating to interfacial oxygen, thus suppressing the reduction and aggregation of Ru (Fig. 6f). On the other hand, the Na$^+$ additives can promote the addition of activated hydrogen species to the substrates by stabilizing the negatively charged intermediates and transition states, experimentally proved by the H$_2$/D$_2$ isotopic study related to H$_2$ activation as the rate-determining step (RDS). However, the presence of Na$^+$ is ineffective in promoting the hydrogenation catalysis when the RDS is H$_2$ activation. The obvious promotion effect of Na$^+$ cations would be observed in the hydrogenation of inert unsaturated substrates with high-barrier hydrogen transfer as the RDS. As expected, Ru(Na) displayed enhanced activity in the hydrogenation of dimethyl oxalate and phenol compared with that of Ru(H).

In addition to vicinal alkali metal sites, doping non-metal elements (e.g., P) into SACs can also facilitate hydrogenation catalysis. For example, Lu and co-workers reported that, with the assistance of P doping, the resulting Pt$_1$/PO$_4$–CeO$_2$ exhibited 10 times higher hydrogenation activity than Pt$_1$/CeO$_2$ for a broad range of substrates (e.g., styrene, cyclohexene, phenylacetylene, and nitrobenzene) (Fig. 6g).[94] Structural characterization indicated that P was bonded to the oxygen atoms on Pt–O moieties to form P–O–Pt coordination. The P species serves as an electron acceptor and induces the charge transfer from Pt to P, endowing Pt single atoms with a more positive charge in Pt$_1$/PO$_4$–CeO$_2$. Taking styrene as the probe molecule, they found that the strong adsorption ability of styrene and hydrogen spillover over Pt$_1$/PO$_4$–CeO$_2$ resulted in remarkable activity enhancement.

3.1.2.3 The effect of surface ligands. For homogeneous catalysts, the coordination environment of metal sites depends on the organic ligands, which is often correlated with the catalytic activity and selectivity. Apart from the role of binding sites in metal centers, the organic ligands also act as proton acceptors in hydrogenation catalysis.[95,96] The great functions of a ligand have inspired the design of highly stable and active SACs. In the case of SACs, the organic ligands can be introduced onto the surface of supports, and the single metal atoms are coordinated to the functional groups (e.g., hydroxyl, thiol, amino, etc.) of organic ligands.[97] DFT calculations proved that the type and concentration of oxygen-containing ligands on the carbon support played a critical role in the electronic structure, stability, and catalytic activity of Pt SACs.[98] Recently, stable atomically dispersed Pd on ethylene glycolate (EG) ligands modified TiO$_2$ was synthesized by a photochemical strategy.[21] When EG-free TiO$_2$ is used as the support, Pd nanoparticles instead of single atoms are formed. Therefore, it can be concluded that the surface EG ligands play a critical role in stabilizing atomically dispersed Pd during the preparation process. Using the hydrogenation of styrene as a probe reaction,
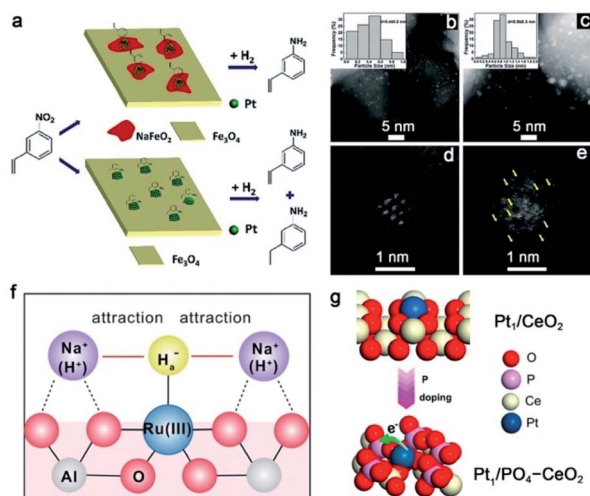

Fig. 6 (a) The proposed mechanism for hydrogenation of 3-nitrostyrene over Na-containing and Na-free Pt/FeO$_x$ catalysts. HAADF-STEM images of (b and d) 2.16% Pt/FeO$_x$ and (c, e) 5.03% Na to 2.16% Pt/FeO$_x$. Reproduced from ref. 92, under terms of Creative Commons license, Published 2017 by Royal Society of Chemistry. (f) Schematic diagram of the role of Na$^+$ cations in stabilizing the Ru(III) species. Reproduced with permission from ref. 93. Copyright 2020, Springer Nature. (g) Schematic illustration of the formation of Pt$_1$/PO$_4$–CeO$_2$ by P doping. Reproduced with permission from ref. 94. Copyright 2019, American Chemical Society.

This journal is © The Royal Society of Chemistry 2022

J. Mater. Chem. A, 2022, 10, 5743–5757 | 5749

Pd$_1$/EG-TiO$_2$ SACs exhibited excellent catalytic activity in the hydrogenation of styrene with a TOF of 8973 h^{-1} at room temperature. It is found that the EG ligands help to activate H$_2$ in a heterolytic manner to produce H$^+$/H$^-$ pairs. The activation barrier for this step is 0.40 eV, and the reaction energy is exothermic by 0.69 eV (Fig. 7a and b). The theoretical and experimental results suggested that the hydrogenation process of styrene began with the transfer of H$^{\delta-}$ from Pd to the terminal CH$_2$ by overcoming a barrier of only 0.47 eV to form the half hydrogenated intermediate. Then, H$^{\delta+}$ from the nearby OH group was added to the half hydrogenated intermediate with a barrier of 0.73 eV, yielding the product (*i.e.*, ethylbenzene). As a comparison, the Pd$_1$/TiO$_2$ SACs without EG ligands displayed a significantly reduced activity with a TOF of only 1930 h^{-1}. Therefore, the unique H$_2$ activation pathway effectively promoted the hydrogenation reaction. As expected, Pd$_1$/EG-TiO$_2$ SACs also showed much better activity in the hydrogenation of polar unsaturated C=O bonds (Fig. 7c).

In addition to the organic groups, inorganic heteropolyacids have been considered as a class of good ligands for single metal species.[99] Specifically, phosphomolybdic acid (H$_3$PMo$_{12}$O$_{40}$, PMA) has a classical Keggin structure, which can offer a variety of coordination sites including the single corner site, bridge site (the O$_c$–O$_{br}$-bridge site), three-fold hollow site (3-H_O$_c$ and 3-H_O$_{br}$), and four-fold hollow site (4-H). For example, Yan and co-workers synthesized a stable Pt$_1$ SAC on PMA-modified active carbon.[100] The DFT results revealed that the Pt atom preferred to bond with four bridging oxygen atoms in the four-fold hollow site with a lower adsorption energy of −5.72 eV compared with other possible coordination sites. The optimized structure of Pt$_1$ on PMA/graphene is shown in Fig. 7d, which has the capacity of stabilizing high loading of Pt single atoms. The XANES and X-ray photoelectron spectroscopy (XPS) results suggested that the charge transfer occurred from Pt to PMA, which made Pt positively charged and thus favored the adsorption of H$_2$. In the

catalytic hydrogenation of nitrobenzene, Pt–PMA/AC exhibited outstanding activity and selectivity (Fig. 7e). Though the TOFs of Pt–PMA/AC (*ca.* 800 h^{-1}) and Pt/AC (*ca.* 900 h^{-1}) were comparable, the selectivity towards aniline showed enormous improvement from only 50% over Pt/AC to 100% over Pt–PMA/AC. The enhanced performance was ascribed to the favorable adsorption and polarization of the intermediates over positively charged Pt. Importantly, Pt–PMA/AC retained the original activity and selectivity over five cycles, implying the high stability of the catalysts.

3.2 Electrocatalytic hydrogenation

Electrocatalytic hydrogenation has emerged as an energy-efficient and environment-friendly method in catalytic transformations. The initial exploration of electrocatalytic hydrogenation can be dated back to the early 20th century, which pioneered the electrochemical reductions of unsaturated compounds in aqueous media.[101–104] The electrocatalytic hydrogenation process involves the generation of absorbed hydrogen (H$_{ads}$) on the cathode by electroreduction of H$_2$O or H$_3$O$^+$, followed by the reaction of an absorbed substrate and H$_{ads}$ on the cathode, and the desorption of the hydrogenated product. Compared with thermal-catalytic hydrogenation, electrocatalytic hydrogenation has several advantages: (1) the H$_{ads}$ originates from the reduction of H$_2$O *via* the Volmer reaction, and thus the supply and mass transport of poorly soluble H$_2$ are bypassed. (2) The H$_{ads}$ is electrochemically generated *in situ* on the cathode surface under mild conditions, without overcoming a high dissociation barrier of H$_2$.[105] (3) The amount of H$_{ads}$ is controlled by changing the applied potential.[106] Therefore, the electrocatalytic hydrogenation reaction can proceed in a greener, milder, and more controllable way. However, the electrocatalytic hydrogenation is always accompanied by the competing hydrogen evolution reaction (HER), leading to the consumption of H$_{ads}$ through Tafel or Heyrovsky reactions and lowering the faradaic efficiency of electrocatalytic hydrogenation.[107] In this section, we take nitrate electroreduction and CO$_2$ electroreduction reactions as typical examples to introduce the recent advances in electrocatalytic hydrogenation.

3.2.1 Nitrate electroreduction. Nitrate (NO$_3^-$) has been considered as one of the most widespread contaminants in surface water and groundwater.[108] The concentration of nitrate keeps increasing due to human activities including over-fertilization and discharge of industrial wastewater, which severely threatens ecological balance and human health.[109–111] Several technologies have been utilized for nitrate degradation, such as biological denitrification,[112] ion exchange[113] and reverse osmosis.[114] However, these technologies suffer from expensive post-treatment, time-consuming processes, and tedious technical problems, limiting their widespread applications.[115,116] Although thermal-catalytic reduction of nitrate can achieve high performance, it heavily relies on the continuous supply of H$_2$, which undoubtedly increases the cost and operation complexity.[117] Alternatively, the electrocatalytic nitrate reduction reaction (NO$_3$RR) is emerging as an environmentally
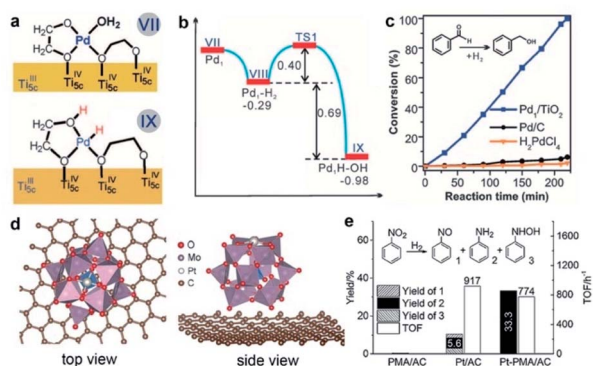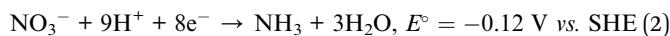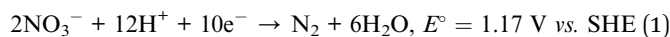

Fig. 7 (a) Models and (b) energies of Pd$_1$/EG-TiO$_2$ and intermediates in the heterolytic H$_2$ activation. (c) Catalytic performances of different catalysts in hydrogenation of benzaldehyde. Reproduced with permission from ref. 21. Copyright 2016, American Association for the Advancement of Science. (d) Top view and side view of the optimized structure of Pt$_1$ on PMA/graphene. (e) Catalytic performances of different catalysts in hydrogenation of nitrobenzene. Reproduced with permission from ref. 100. Copyright 2016 John Wiley and Sons.

5750 | *J. Mater. Chem. A*, 2022, **10**, 5743–5757

This journal is © The Royal Society of Chemistry 2022

friendly and sustainable strategy to remove nitrate contaminants because of its several benefits, such as the renewable energy (*i.e.*, electricity) as the driving force, simple operation conditions, and no need of post-processing.[118–120]

3.2.1.1 Reaction pathways of nitrate electroreduction. As nitrogen (N) contains a wide range of oxidation valences from +5 to −3, nitrate can be electrocatalytically reduced to a variety of nitrogen-containing intermediates or products, such as NO_2^-, NO, N_2O, N_2, NH_2OH, and NH_3. Hence, the NO_3RR is a complex multi-electron-involving process. In terms of the reaction pathways, the NO_3RR can be classified as an indirect autocatalytic reduction pathway and direct electrocatalytic reduction pathway (Fig. 8).[121] The indirect autocatalytic reduction pathway means that NO_2 or NO^+ instead of nitrate participates in the electron-transfer process, and it only proceeds under the highly acidic media conditions in the presence of nitrate (>1 M) and nitrite or highly concentrated nitric acid solutions (>4 M).[122–124] Generally, the NO_3RR at low concentrations (below 1 M) is carried out through a direct electrocatalytic reduction pathway, including absorbed hydrogen reduction and electron reduction routes (Fig. 9).[125] The main products are N_2 and NH_3 because of their high thermodynamical stability. The specific reactions are shown as follows (eqn (1) and (2)):[110]

$$2NO_3^- + 12H^+ + 10e^- \rightarrow N_2 + 6H_2O, \ E^\circ = 1.17 \ V \ vs. \ SHE \quad (1)$$

$$NO_3^- + 9H^+ + 8e^- \rightarrow NH_3 + 3H_2O, \ E^\circ = -0.12 \ V \ vs. \ SHE \quad (2)$$

In the adsorbed hydrogen-mediated route, the generation of H_{ads} *via* the reduction of H_2O initiates the reaction. Due to strong reducing ability of H_{ads}, the absorbed nitrate is reduced by the stepwise H_{ads} addition *via* a variety of intermediates such as $NO_2^-_{ads}$, NO_{ads}, N_{ads}, NH_{ads}, and NH_{2ads}. As a result, the
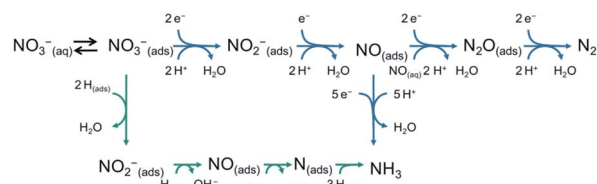
Fig. 9 The electron and absorbed hydrogen mediated direct electrocatalytic routes for the NO_3RR. Reproduced with permission from ref. 125. Copyright 2021 Elsevier.

dominant product is NH_3 instead of N_2, because the much lower migration barrier (0.10 eV) of H_{ads} than that of N_{ads} (0.75 eV) kinetically favors the formation of the N–H bond compared with the N–N bond.[126]

In the electron reduction route, the absorbed nitrate is first reduced to nitrite ($NO_2^-_{ads}$), which is the rate-determining step. The reaction rate strongly depends on the concentration of nitrate. At low concentrations (<0.1 M), the reaction order of nitrate is positive. The main factor that influences the reaction rate is the competing co-adsorption of anions (*e.g.*, sulfate) from the electrolyte.[122] At high concentrations (>0.1 M), the reaction order is negative. This is most likely caused by the fact that the high coverage of nitrate impedes the absorption of other necessary species (*e.g.*, water), highlighting the critical role of free surface sites in the reaction rate.[122] The second step is the reduction of $NO_2^-_{ads}$ into NO_{ads}. The NO_{ads} is a key intermediate for the end products. When NO_{ads} is directly reduced, the end product is NH_3 *via* the intermediates of HNO_{ads}, H_2NO_{ads}, and NH_2OH_{ads}. When NO_{ads} reacts with NO dissolved in solution (NO_{aq}), the end product is N_2 *via* the intermediate of N_2O_{ads}. In addition, N_2 can also be produced *via* other intermediates from the reduction of NO_{ads}, such as N_{ads}, or NH_{2ads}.[121]

3.2.1.2 Mechanism of nitrate electroreduction over SACs. Selectively converting nitrate into environmentally friendly N_2 or value-added NH_3 through the electrocatalytic NO_3RR has been a promising approach to mitigate environmental concerns and obtain chemical products. However, the NO_3RR involves a multi-electron-/proton transfer process for the generation of N_2 and NH_3, leading to the slow reaction kinetics. Moreover, besides the competing NO_3^--to-N_2 reaction, the conversion of NO_3^- into NH_3 is often accompanied by the generation of H_2 through the HER, resulting in low faradaic efficiency.[127–129] Therefore, it is desirable to explore efficient and selective NO_3RR electrocatalysts to improve the reaction rate and obtain exclusive products.

Due to the unique electronic properties and structural homogeneity of active sites, SACs exhibit high catalytic activity and selectivity in many fields. As expected, SACs hold great promise as excellent electrocatalysts towards the NO_3RR. Guo and co-workers used DFT calculations to predict the promising potential of SACs in the NO_3RR.[130] Using the adsorption energy of NO_3^- (ΔG_{*NO_3}) as a descriptor, they found that Ti/g-CN and Zr/g-CN stood out with low limiting potentials of −0.39 and −0.41 V *vs.* the reversible hydrogen electrode (RHE),
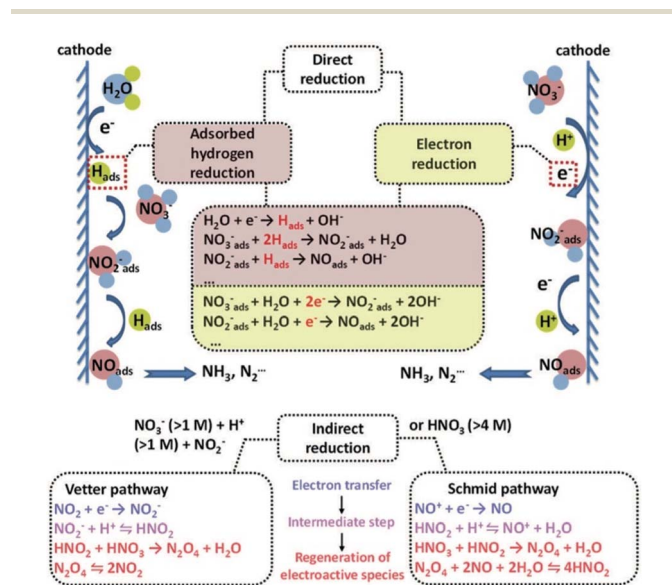

Fig. 8 The proposed reaction pathways for the NO_3RR. Reproduced with permission from ref. 121. Copyright 2021 The Royal Society of Chemistry.

This journal is © The Royal Society of Chemistry 2022

J. Mater. Chem. A, 2022, **10**, 5743–5757 | 5751

respectively, among a variety of transition metal (from Ti to Au) SACs supported on graphitic carbon nitrides (g-CN). Ti/g-CN and Zr/g-CN SACs can also achieve high-selectivity for the NO_3RR towards NH_3, because large energy barriers impede the formation of byproducts (NO_2, NO, N_2O, and N_2). Moreover, the adsorption strength of NO_3^- on Ti/g-CN and Zr/g-CN is stronger than that of the H proton, confirming the NO_3RR as favorable compared to the competing HER. This work provides theoretical validation for SACs as promising NO_3RR electrocatalysts with high activity and selectivity.

Wang and co-workers synthesized Fe SACs with the Fe–N coordination configuration on the carbon matrix by a pyrolysis-etching-pyrolysis strategy.[131] The Fe SACs exhibited high-efficiency NO_3RR activity with a high faradaic efficiency of about 75% and a remarkable yield rate of 20 000 $\mu g \ h^{-1} \ mg_{cat.}^{-1}$ at −0.85 V, which is much superior to those of the Fe nanoparticle catalyst (Fig. 10a and b). In addition, the catalyst showed long-term durability after 20 consecutive cycles. DFT calculations revealed Fe–N_4 centers in Fe SACs as highly active sites exhibiting much lower thermodynamic barriers, which are responsible for the outstanding NO_3RR performance. A similar enhancement effect of Fe–N centers for the NO_3RR is also reported in the FeN_x site/Fe nanoparticle system.[132] Liu and co-

workers reported atomically dispersed Fe atoms anchored on S and N-codoped carbon for efficient NO_3RR.[133] Theoretical and experimental investigations suggested that S-doping created more defects on the N-doped carbon basal plane, which is beneficial to the stabilization of single Fe atoms. Moreover, S-modification can regulate the coordination environments of single Fe atoms, forming a FeN_4S_2 coordination structure as the dominating active site of the Fe SAC, and improve the basal conductivity. Benefiting from these advantages, the S-modified Fe SACs exhibited high-efficiency NO_3RR activity, achieving a maximum nitrate removal capacity of 7822 mg N g^{-1} Fe and a high faradaic efficiency of 78.4% at a low potential of −0.57 V vs. RHE, for N_2 production with 100% selectivity. In addition, the catalyst had good cycling stability with ignorable change after 100 cycles. Yu and co-workers reported a polymer-hydrogel strategy to synthesize N-coordinated single Fe sites on carbon for efficient NO_3RR.[127] The catalyst exhibited a maximum NH_3 yield rate of 2.75 mg h^{-1} cm^{-2} with nearly 100% faradaic efficiency. They used surface interrogation scanning electrochemical microscopy (SI-SECM) to investigate the site density of Fe moieties with a dynamic oxidation state by recording the passed charge amounts (Fig. 10c). The transformations of Fe(III/II) in the potential range of 0.8–0.9 V and Fe(II/0) in the potential range of −0.1–0 V are observed for the Fe SAC (Fig. 10d). The potential ranges for the redox behaviors of the Fe–N_x moiety in Fe SACs are more positive and narrower than those in Fe nanoparticles, highlighting the unique thermodynamic and kinetic properties of Fe SACs. They attributed the excellent NO_3RR activity and selectivity of Fe SACs to the preoccupied mechanism of NO_3^- at the Fe(II) site prior to the formation of Fe(0), impeding the competitive HER that usually occurred in bulk catalysts (Fig. 10d). As a result, Fe SACs exhibited a remarkable TOF of 0.7 s^{-1} at 0.7 V in contrast with that of Fe nanoparticles (0.06 s^{-1}) (Fig. 10e).

Besides atomically dispersed Fe sites as active centers for the NO_3RR, single Cu sites have been reported to catalyze the NO_3RR. Feng and co-workers reported a highly active and selective NO_3RR catalyst composed of single Cu atoms anchored on nitrogenated carbon nanosheets (Cu–N–C) by pyrolysis of a Cu-based metal–organic framework.[134] AC-STEM and XAFS analysis confirmed the successful synthesis of the Cu–N–C catalyst with atomically dispersed Cu–N_2 and Cu–N_4 mixed coordination structures. Compared to the Cu plate, Cu–N–C exhibited better activity and stability towards the NO_3RR. Apart from NO_3^-, the absorption of NO_2^- originating from the reduction of NO_3^- also played a significant role in facilitating the NO_3RR. DFT calculations demonstrated that the adsorption of NO_3^- and NO_2^- on Cu–N_x active sites (particularly Cu–N_2) in Cu–N–C is more favorable than that on the Cu(111) plane in the Cu nanoparticles, suppressing the release of nitrite into the solution, which is confirmed by kinetic measurements. In addition, the Cu–N–C catalysts showed outstanding stability after 20 consecutive cycles.

3.2.2 CO_2 electroreduction. The ever-increasing CO_2 release has caused a severe global warming issue. The conversion of CO_2 into value-added chemicals and fuels represents a promising way for maintaining carbon neutrality.[3]
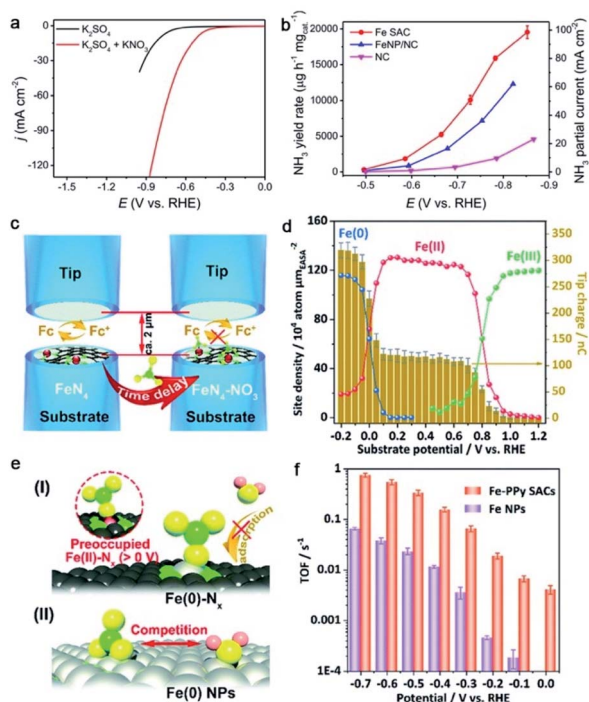

Fig. 10 (a) Polarization curves of the Fe SAC in K_2SO_4 electrolyte with and without KNO_3. (b) NH_3 yield rate and partial current density of the Fe SAC and its counterparts. Reproduced from ref. 131, under the terms of Creative Commons license, published 2021 Springer Nature. (c) The schematic illustration of the SI-SECM setup for identifying Fe sites. (d) The active site density and corresponding titration charges of Fe SACs at different potentials. (e) The proposed NO_3RR mechanism on the Fe SAC and bulk surface. (f) TOFs of Fe SACs and Fe nanoparticles for the NO_3RR. Reproduced with permission from ref. 127. Copyright 2021 The Royal Society of Chemistry.

5752 | J. Mater. Chem. A, 2022, **10**, 5743–5757

This journal is © The Royal Society of Chemistry 2022

Electrocatalytic CO_2 reduction (ECR) using H_2O as a hydrogen source provides a potential strategy for CO_2 reutilization to reduce the CO_2 level. The ECR process is generally considered to be divided into three elementary steps, including the adsorptive activation of CO_2 molecules, the formation of intermediates by proton/electron transfer, and the production and desorption of products.[135,136] Recently, SACs have boomed in the field of ECR due to their unique structures and remarkable electrocatalytic performance. Different types of SACs exhibited distinct reaction pathways and product distributions (such as CO, $HCOO^-$, CH_4, CH_3OH, and even C_{2+} products). For example, Chen and co-workers synthesized N-doped carbon supported single-atom $Co-N_5$ sites as ECR electrocatalysts, which showed nearly 100% CO selectivity and high stability.[137] Zhang and co-workers reported $In^{\delta+}-N_4$ SACs for CO_2 electroreduction to formate with a faradaic efficiency of 96% at -0.65 V vs. RHE.[138] Xin and co-workers showed that single Zn atoms supported on N-doped carbon as the ECR electrocatalyst exhibited a high faradaic efficiency of 85% for CH_4.[139] Zheng and co-workers reported that the neighboring $Cu-N_2$ single-atomic sites can favor the formation of C_2H_4, while the isolated $Cu-N_2$ site was prone to generate C_1 products.[140] As the recent progress in SACs for ECR had been well reported in many excellent reviews,[135,141–144] it was not described in detail here.

4. Summary and perspectives

Thermal- and electro-catalytic hydrogenation reactions are important transformations in the chemical, energy and environmental industries. The development of advanced catalysts is of significance to achieve high activity and selectivity for both thermal- and electro-catalytic hydrogenation transformations. SACs represent the maximum utilization efficiency of metal atoms, providing a promising opportunity for constructing cost-effective catalysts, in particular noble metal catalysts. With 100% exposed active sites and unique electronic structures, SACs exhibit remarkable catalytic activity and selectivity. Furthermore, structural simplicity and homogeneity of SACs can offer ultimate facileness for identifying the structure of catalytically active sites and facilitate a comprehensive understanding of the catalytic process and reaction mechanism, and in turn guides the rational design of high-efficiency catalysts. In this study, SACs are shown to act as promising catalysts in hydrogenation transformations.

Although great progress has been made in the SAC-catalyzed hydrogenation reaction via both thermal- and electro-catalytic routes, some challenges and promising opportunities should be considered in terms of fundamental research and practical applications:

(1) A large number of SACs have been successfully applied to the thermal-catalytic hydrogenation of unsaturated groups, such as C=C, C≡C, C=O, C=N, and N=O bonds. However, limited SACs are developed for electrocatalytic hydrogenation, especially for the NO_3RR, though specific SACs with high-efficiency performance have already been predicted theoretically.[130] Therefore, the exploration of smart synthetic methods for development of SACs with a controlled coordination environment of metal atoms is highly desirable. This is also highly expected to achieve large-scale synthesis to meet the demand of practical applications.

(2) The fabrication of SACs with both excellent activity and stability is highly desired in the field of catalysis. Increased single-atom metal-support interaction (SAMSI) is beneficial for the stabilization of SACs, however, excessively strong SAMSI is often accompanied by a certain reduction in reaction activity.[145,146] Therefore, more efforts should be made to break the activity–stability seesaw effect of SACs. For example, the exploration of single atom alloy or trimer catalysts with synergistic functions of different sites is an urgent need to achieve high activity without compromising the stability for thermal-/electro-catalytic hydrogenations.[69,147]

(3) It has been well accepted that the regulation of electronic structures of metal sites in SACs predominates catalytic performance. It should be noted that the catalytic process not only involves the participation of metal centers, but also is assisted by potential active centers, or other functional atoms through structural effects in the first and second coordination spheres. However, current studies mostly pay little attention to the regulation of the second coordination spheres and its effects on catalytic kinetics, especially for electrocatalytic hydrogenation (e.g., NO_3RR). Therefore, one needs to design and synthesize SACs at the molecular level through second coordination sphere engineering to further optimize the hydrogenation performance.

(4) A comprehensive understanding of the structure–property relationship at the molecular level is the foundation for the rational design of SACs and the further enhancement of catalytic performance. The big challenge lies in advancing the investigation of actual active sites, including the kinetic evolution under reaction conditions, and the associated reaction paths. Therefore, promoting the development of theoretical computation and in situ characterization technologies, such as in situ electron microscopy, in situ XAFS, and in situ electrochemical characterization techniques is in great demand. In addition, kinetics measurements should be conducted for gaining a deep insight into the reaction mechanism.[127,148]

Conflicts of interest

There are no conflicts to declare.

Acknowledgements

References

1 P. Grange, *Catal. Rev.: Sci. Eng.*, 1980, 135–181.
2 T. C. Ho, *Catal. Rev.: Sci. Eng.*, 1988, **30**, 117–160.

This journal is © The Royal Society of Chemistry 2022

J. Mater. Chem. A, 2022, **10**, 5743–5757 | **5753**

3 X. Jiang, X. Nie, X. Guo, C. Song and J. G. Chen, *Chem. Rev.*, 2020, **120**, 7984–8034.

4 W. Wang, S. Wang, X. Ma and J. Gong, *Chem. Soc. Rev.*, 2011, **40**, 3703–3727.

5 L. Alig, M. Fritz and S. Schneider, *Chem. Rev.*, 2019, **119**, 2681–2751.

6 Y. Zhai, Z. Zhu, C. Zhu, K. Chen, X. Zhang, J. Tang and J. Chen, *Mater. Today*, 2020, **38**, 99–113.

7 R. Jia, Y. Wang, C. Wang, Y. Ling, Y. Yu and B. Zhang, *ACS Catal.*, 2020, **10**, 3533–3540.

8 X. Yan, D. Liu, H. Cao, F. Hou, J. Liang and S. X. Dou, *Small Methods*, 2019, **3**, 1800501.

9 S. Lux, G. Baldauf-Sommerbauer and M. Siebenhofer, *ChemSusChem*, 2018, **11**, 3357–3375.

10 P. Sharma, J. Sebastian, S. Ghosh, D. Creaser and L. Olsson, *Catal. Sci. Technol.*, 2021, **11**, 1665–1697.

11 X. Liu, C.-Y. Mou, S. Lee, Y. Li, J. Secrest and B. W. L. Jang, *J. Catal.*, 2012, **285**, 152–159.

12 N. Singh, Y. Song, O. Y. Gutiérrez, D. M. Camaioni, C. T. Campbell and J. A. Lercher, *ACS Catal.*, 2016, **6**, 7466–7470.

13 L. Zhang, M. Zhou, A. Wang and T. Zhang, *Chem. Rev.*, 2019, **120**, 683–733.

14 A. Wang, J. Li and T. Zhang, *Nat. Rev. Chem.*, 2018, **2**, 65–81.

15 K. Liu, R. Qin and N. Zheng, *J. Am. Chem. Soc.*, 2021, **143**, 4483–4499.

16 G. Hamm, T. Schmidt, J. Breitbach, D. Franke, C. Becker and K. Wandelt, *Z. Phys. Chem.*, 2009, **223**, 209–232.

17 M. Li and J. Shen, *Thermochim. Acta*, 2001, **379**, 45–50.

18 H. Zhou, X. Yang, L. Li, X. Liu, Y. Huang, X. Pan, A. Wang, J. Li and T. Zhang, *ACS Catal.*, 2016, **6**, 1054–1061.

19 F. Studt, F. Abild-Pedersen, T. Bligaard, R. Z. Sørensen, C. H. Christensen and J. K. Nørskov, *Science*, 2008, **320**, 1320–1322.

20 J. Zhang, C. Liu and B. Zhang, *Small Methods*, 2019, **3**, 1800481.

21 P. Liu, Y. Zhao, R. Qin, S. Mo, G. Chen, L. Gu, D. M. Chevrier, P. Zhang, Q. Guo, D. Zang, B. Wu, G. Fu and N. Zheng, *Science*, 2016, **352**, 797–801.

22 B. Qiao, A. Wang, X. Yang, L. F. Allard, Z. Jiang, Y. Cui, J. Liu, J. Li and T. Zhang, *Nat. Chem.*, 2011, **3**, 634–641.

23 Y. Peng, B. Lu and S. Chen, *Adv. Mater.*, 2018, **30**, 1801995.

24 L. Liu and A. Corma, *Chem. Rev.*, 2018, **118**, 4981–5079.

25 R. Vanharde and F. Hartog, *Surf. Sci.*, 1969, **15**, 189–230.

26 N. Lopez, T. V. W. Janssens, B. S. Clausen, Y. Xu, M. Mavrikakis, T. Bligaard and J. K. Nørskov, *J. Catal.*, 2004, **223**, 232–235.

27 X.-F. Yang, A. Wang, B. Qiao, J. Li, J. Liu and T. Zhang, *Acc. Chem. Res.*, 2013, **46**, 1740–1748.

28 M. Valden, X. Lai and D. W. Goodman, *Science*, 1998, **281**, 1647–1650.

29 E. Roduner, *Chem. Soc. Rev.*, 2006, **35**, 583–592.

30 B. Yoon, H. Häkkinen, U. Landman, A. S. Wörz, J.-M. Antonietti, S. Abbet, K. Judai and U. Heiz, *Science*, 2005, **307**, 403–407.

31 C. T. Campbell, *Nat. Chem.*, 2012, **4**, 597–598.

32 B. Qiao, J. Liu, Y.-G. Wang, Q. Lin, X. Liu, A. Wang, J. Li, T. Zhang and J. Liu, *ACS Catal.*, 2015, **5**, 6249–6254.

33 X. Chen, M. Peng, X. Cai, Y. Chen, Z. Jia, Y. Deng, B. Mei, Z. Jiang, D. Xiao, X. Wen, N. Wang, H. Liu and D. Ma, *Nat. Commun.*, 2021, **12**, 2664.

34 P. Li, M. Wang, X. Duan, L. Zheng, X. Cheng, Y. Zhang, Y. Kuang, Y. Li, Q. Ma, Z. Feng, W. Liu and X. Sun, *Nat. Commun.*, 2019, **10**, 1711.

35 Z. Luo, Y. Ouyang, H. Zhang, M. Xiao, J. Ge, Z. Jiang, J. Wang, D. Tang, X. Cao, C. Liu and W. Xing, *Nat. Commun.*, 2018, **9**, 2120.

36 S. Li, Y. Xu, Y. Chen, W. Li, L. Lin, M. Li, Y. Deng, X. Wang, B. Ge, C. Yang, S. Yao, J. Xie, Y. Li, X. Liu and D. Ma, *Angew. Chem., Int. Ed.*, 2017, **56**, 10761–10765.

37 Y. Chen, S. Ji, C. Chen, Q. Peng, D. Wang and Y. Li, *Joule*, 2018, **2**, 1242–1264.

38 L. Jiao and H.-L. Jiang, *Chem*, 2019, **5**, 786–804.

39 S. Abbet, A. Sanchez, U. Heiz, W.-D. Schneider, A. M. Ferrari, G. Pacchioni and N. Rösch, *J. Am. Chem. Soc.*, 2000, **122**, 3453–3457.

40 H. Yan, H. Cheng, H. Yi, Y. Lin, T. Yao, C. Wang, J. Li, S. Wei and J. Lu, *J. Am. Chem. Soc.*, 2015, **137**, 10484–10487.

41 B. J. O'Neill, D. H. K. Jackson, J. Lee, C. Canlas, P. C. Stair, C. L. Marshall, J. W. Elam, T. F. Kuech, J. A. Dumesic and G. W. Huber, *ACS Catal.*, 2015, **5**, 1804–1825.

42 G. Liu, A. W. Robertson, M. M. Li, W. C. H. Kuo, M. T. Darby, M. H. Muhieddine, Y. C. Lin, K. Suenaga, M. Stamatakis, J. H. Warner and S. C. E. Tsang, *Nat. Chem.*, 2017, **9**, 810–816.

43 J. Zhang, X. Wu, W.-C. Cheong, W. Chen, R. Lin, J. Li, L. Zheng, W. Yan, L. Gu, C. Chen, Q. Peng, D. Wang and Y. Li, *Nat. Commun.*, 2018, **9**, 1002.

44 J. Wan, W. Chen, C. Jia, L. Zheng, J. Dong, X. Zheng, Y. Wang, W. Yan, C. Chen, Q. Peng, D. Wang and Y. Li, *Adv. Mater.*, 2018, **30**, 1705369.

45 Y. Chen, S. Ji, Y. Wang, J. Dong, W. Chen, Z. Li, R. Shen, L. Zheng, Z. Zhuang, D. Wang and Y. Li, *Angew. Chem., Int. Ed.*, 2017, **56**, 6937–6941.

46 X. Wang, W. Chen, L. Zhang, T. Yao, W. Liu, Y. Lin, H. Ju, J. Dong, L. Zheng, W. Yan, X. Zheng, Z. Li, X. Wang, J. Yang, D. He, Y. Wang, Z. Deng, Y. Wu and Y. Li, *J. Am. Chem. Soc.*, 2017, **139**, 9419–9422.

47 J. D. Kistler, N. Chotigkrai, P. Xu, B. Enderle, P. Praserthdam, C. Y. Chen, N. D. Browning and B. C. Gates, *Angew. Chem., Int. Ed.*, 2014, **53**, 8904–8907.

48 H. Wu, H. Li, X. Zhao, Q. Liu, J. Wang, J. Xiao, S. Xie, R. Si, F. Yang, S. Miao, X. Guo, G. Wang and X. Bao, *Energy Environ. Sci.*, 2016, **9**, 3736–3745.

49 H. Fei, J. Dong, M. J. Arellano-Jimenez, G. Ye, N. Dong Kim, E. L. Samuel, Z. Peng, Z. Zhu, F. Qin, J. Bao, M. J. Yacaman, P. M. Ajayan, D. Chen and J. M. Tour, *Nat. Commun.*, 2015, **6**, 8668.

50 H. Fei, J. Dong, Y. Feng, C. S. Allen, C. Wan, B. Volosskiy, M. Li, Z. Zhao, Y. Wang, H. Sun, P. An, W. Chen, Z. Guo, C. Lee, D. Chen, I. Shakir, M. Liu, T. Hu, Y. Li, A. I. Kirkland, X. Duan and Y. Huang, *Nat. Catal.*, 2018, **1**, 63–72.

5754 | *J. Mater. Chem. A*, 2022, **10**, 5743–5757

This journal is © The Royal Society of Chemistry 2022

51 V. Madhavan, W. Chen, T. Jamneala, M. F. Crommie and N. S. Wingreen, *Science*, 1998, **280**, 567–569.

52 D. Deng, X. Chen, L. Yu, X. Wu, Q. Liu, Y. Liu, H. Yang, H. Tian, Y. Hu, P. Du, R. Si, J. Wang, X. Cui, H. Li, J. Xiao, T. Xu, J. Deng, F. Yang, P. N. Duchesne, P. Zhang, J. Zhou, L. Sun, J. Li, X. Pan and X. Bao, *Sci. Adv.*, 2015, **1**, e1500462.

53 Z. Miao, X. Wang, M. C. Tsai, Q. Jin, J. Liang, F. Ma, T. Wang, S. Zheng, B. J. Hwang, Y. Huang, S. Guo and Q. Li, *Adv. Energy Mater.*, 2018, **8**, 1801226.

54 M. Zhang, Y. G. Wang, W. Chen, J. Dong, L. Zheng, J. Luo, J. Wan, S. Tian, W. C. Cheong, D. Wang and Y. Li, *J. Am. Chem. Soc.*, 2017, **139**, 10976–10979.

55 A. S. Hoffman, C.-Y. Fang and B. C. Gates, *J. Phys. Chem. Lett.*, 2016, **7**, 3854–3860.

56 J. Liu, F. R. Lucci, M. Yang, S. Lee, M. D. Marcinkowski, A. J. Therrien, C. T. Williams, E. C. Sykes and M. Flytzani-Stephanopoulos, *J. Am. Chem. Soc.*, 2016, **138**, 6396–6399.

57 Z. W. Seh, J. Kibsgaard, C. F. Dickens, I. Chorkendorff, J. K. Nørskov and T. F. Jaramillo, *Science*, 2017, **355**, eaad4998.

58 K. Brandt, M. E. Chiu, D. J. Watson, M. S. Tikhov and R. M. Lambert, *J. Phys. Chem. C*, 2012, **116**, 4605–4611.

59 H. Qi, J. Yang, F. Liu, L. Zhang, J. Yang, X. Liu, L. Li, Y. Su, Y. Liu, R. Hao, A. Wang and T. Zhang, *Nat. Commun.*, 2021, **12**, 3295.

60 K. Jiang, S. Back, A. J. Akey, C. Xia, Y. Hu, W. Liang, D. Schaak, E. Stavitski, J. K. Nørskov, S. Siahrostami and H. Wang, *Nat. Commun.*, 2019, **10**, 3997.

61 S. Yang, Y. J. Tak, J. Kim, A. Soon and H. Lee, *ACS Catal.*, 2017, **7**, 1301–1307.

62 H.-Y. T. Chen, S. Tosoni and G. Pacchioni, *ACS Catal.*, 2015, **5**, 5486–5495.

63 E. A. I. Shor, V. A. Nasluzov, A. M. Shor, G. N. Vayssilov and N. Rösch, *J. Phys. Chem. C*, 2007, **111**, 12340–12351.

64 J. A. Santana and N. Rösch, *Phys. Chem. Chem. Phys.*, 2012, **14**, 16062–16069.

65 M. Zhou, M. Yang, X. Yang, X. Zhao, L. Sun, W. Deng, A. Wang, J. Li and T. Zhang, *Chin. J. Catal.*, 2020, **41**, 524–532.

66 O. Eisenstein and R. H. Crabtree, *New J. Chem.*, 2013, **37**, 21–27.

67 G. Vile, D. Albani, M. Nachtegaal, Z. Chen, D. Dontsova, M. Antonietti, N. López and J. Pérez-Ramírez, *Angew. Chem., Int. Ed.*, 2015, **54**, 11265–11269.

68 P. Liu and N. Zheng, *Natl. Sci. Rev.*, 2018, **5**, 636–638.

69 G. Kyriakou, M. B. Boucher, A. D. Jewell, E. A. Lewis, T. J. Lawton, A. E. Baber, H. L. Tierney, M. Flytzani-Stephanopoulos and E. C. H. Sykes, *Science*, 2012, **335**, 1209–1212.

70 Y. Xu, M. Chu, F. Liu, X. Wang, Y. Liu, M. Cao, J. Gong, J. Luo, H. Lin, Y. Li and Q. Zhang, *Nano Lett.*, 2020, **20**, 6865–6872.

71 K. Liu, R. Qin, L. Zhou, P. Liu, Q. Zhang, W. Jing, P. Ruan, L. Gu, G. Fu and N. Zheng, *CCS Chem.*, 2019, **1**, 207–214.

72 Y. Ren, Y. Tang, L. Zhang, X. Liu, L. Li, S. Miao, D. Sheng Su, A. Wang, J. Li and T. Zhang, *Nat. Commun.*, 2019, **10**, 4500.

73 Y. Ma, Y. Ren, Y. Zhou, W. Liu, W. Baaziz, O. Ersen, C. Pham-Huu, M. Greiner, W. Chu, A. Wang, T. Zhang and Y. Liu, *Angew. Chem., Int. Ed.*, 2020, **59**, 21613–21619.

74 Y. Cao, J. Guerrero-Sánchez, I. Lee, X. Zhou, N. Takeuchi and F. Zaera, *ACS Catal.*, 2020, **10**, 3431–3443.

75 J. Zhang, C. Zheng, M. Zhang, Y. Qiu, Q. Xu, W.-C. Cheong, W. Chen, L. Zheng, L. Gu, Z. Hu, D. Wang and Y. Li, *Nano Res.*, 2020, **13**, 3082–3087.

76 X. Long, Z. Li, G. Gao, P. Sun, J. Wang, B. Zhang, J. Zhong, Z. Jiang and F. Li, *Nat. Commun.*, 2020, **11**, 4074.

77 W. Liu, L. Zhang, X. Liu, X. Liu, X. Yang, S. Miao, W. Wang, A. Wang and T. Zhang, *J. Am. Chem. Soc.*, 2017, **139**, 10790–10798.

78 X. Wang, Z. Chen, X. Zhao, T. Yao, W. Chen, R. You, C. Zhao, G. Wu, J. Wang, W. Huang, J. Yang, X. Hong, S. Wei, Y. Wu and Y. Li, *Angew. Chem., Int. Ed.*, 2018, **57**, 1944–1948.

79 J. Lu, P. Serna, C. Aydin, N. D. Browning and B. C. Gates, *J. Am. Chem. Soc.*, 2011, **133**, 16186–16195.

80 C. Tang, L. Chen, H. Li, L. Li, Y. Jiao, Y. Zheng, H. Xu, K. Davey and S. Z. Qiao, *J. Am. Chem. Soc.*, 2021, **143**, 7819–7827.

81 W. Li, F. Li, H. Yang, X. Wu, P. Zhang, Y. Shan and L. Sun, *Nat. Commun.*, 2019, **10**, 5074.

82 J. Doebereiner, *Ann. Phys.*, 1845, **140**, 94–96.

83 F. J. Williams, A. Palermo, S. Tracey, M. S. Tikhov and R. M. Lambert, *J. Phys. Chem. B*, 2002, **106**, 5668–5672.

84 N. Mahata, K. V. Raghavan and V. Vishwanathan, *Appl. Catal., A*, 1999, **182**, 183–187.

85 W. D. Mross, *Catal. Rev.: Sci. Eng.*, 1983, **25**, 591–637.

86 S. R. d. Miguel, A. A. Castro, O. A. Scelza and J. Soria, *Catal. Lett.*, 1995, **32**, 281–291.

87 Y. Chai, G. Wu, X. Liu, Y. Ren, W. Dai, C. Wang, Z. Xie, N. Guan and L. Li, *J. Am. Chem. Soc.*, 2019, **141**, 9920–9927.

88 M. Yang, J. Liu, S. Lee, B. Zugic, J. Huang, L. F. Allard and M. Flytzani-Stephanopoulos, *J. Am. Chem. Soc.*, 2015, **137**, 3470–3473.

89 M. Yang, S. Li, Y. Wang, J. A. Herron, Y. Xu, L. F. Allard, S. Lee, J. Huang, M. Mavrikakis and M. Flytzani-Stephanopoulos, *Science*, 2014, **346**, 1498–1501.

90 J. Lin, A. Wang, B. Qiao, X. Liu, X. Yang, X. Wang, J. Liang, J. Li, J. Liu and T. Zhang, *J. Am. Chem. Soc.*, 2013, **135**, 15314–15317.

91 H. Wei, X. Liu, A. Wang, L. Zhang, B. Qiao, X. Yang, Y. Huang, S. Miao, J. Liu and T. Zhang, *Nat. Commun.*, 2014, **5**, 5634.

92 H. Wei, Y. Ren, A. Wang, X. Liu, X. Liu, L. Zhang, S. Miao, L. Li, J. Liu, J. Wang, G. Wang, D. Su and T. Zhang, *Chem. Sci.*, 2017, **8**, 5126–5131.

93 R. Qin, L. Zhou, P. Liu, Y. Gong, K. Liu, C. Xu, Y. Zhao, L. Gu, G. Fu and N. Zheng, *Nat. Catal.*, 2020, **3**, 703–709.

94 Y. Ma, B. Chi, W. Liu, L. Cao, Y. Lin, X. Zhang, X. Ye, S. Wei and J. Lu, *ACS Catal.*, 2019, **9**, 8404–8412.

95 W. W. N. O and R. H. Morris, *ACS Catal.*, 2013, **3**, 32–40.

96 N. M. Rezayee, D. C. Samblanet and M. S. Sanford, *ACS Catal.*, 2016, **6**, 6377–6383.

This journal is © The Royal Society of Chemistry 2022

J. Mater. Chem. A, 2022, **10**, 5743–5757 | 5755

97 Y. T. Kim, T. Uruga and T. Mitani, *Adv. Mater.*, 2006, **18**, 2634–2638.

98 M. Mahmoodinia, P.-O. Åstrand and D. Chen, *J. Phys. Chem. C*, 2017, **121**, 20802–20812.

99 P. He, B. Xu, X. Xu, L. Song and X. Wang, *Chem. Sci.*, 2016, **7**, 1011–1015.

100 B. Zhang, H. Asakura, J. Zhang, J. Zhang, S. De and N. Yan, *Angew. Chem., Int. Ed.*, 2016, **55**, 8319–8323.

101 S. Fokin, *Z. Elektrochem.*, 1906, **12**, 749–762.

102 F. Fichter and R. Stocker, *Chem. Ber.*, 1914, **47**, 2015.

103 U. Pomilio, *Z. Elektrochem.*, 1915, **21**, 444.

104 W. M. Leslie and J. A. V. Butler, *Trans. Faraday Soc.*, 1936, **32**, 989–998.

105 J. Lessard, in *Organic Electrochemistry*, ed. O. Hammerich and B. Speiser, CRC Press, 5th edn, 2015, pp. 1658–1664.

106 J. M. Chapuzet, A. Lasia and J. Lessard, in *Electrocatalysis*, ed. J. Lipkowski and P. N. Ross, Wiley-VCH, 1998, pp. 155–196.

107 X. H. Chadderdon, D. J. Chadderdon, J. E. Matthiesen, Y. Qiu, J. M. Carraher, J.-P. Tessonnier and W. Li, *J. Am. Chem. Soc.*, 2017, **139**, 14120–14128.

108 J. G. Chen, R. M. Crooks, L. C. Seefeldt, K. L. Bren, R. M. Bullock, M. Y. Darensbourg, P. L. Holland, B. Hoffman, M. J. Janik, A. K. Jones, M. G. Kanatzidis, P. King, K. M. Lancaster, S. V. Lymar, P. Pfromm, W. F. Schneider and R. R. Schrock, *Science*, 2018, **360**, eaar6611.

109 J. Martínez, A. Ortiz and I. Ortiz, *Appl. Catal., B*, 2017, **207**, 42–59.

110 S. Garcia-Segura, M. Lanzarini-Lopes, K. Hristovski and P. Westerhoff, *Appl. Catal., B*, 2018, **236**, 546–568.

111 N. Lehnert, H. T. Dong, J. B. Harland, A. P. Hunt and C. J. White, *Nat. Rev. Chem.*, 2018, **2**, 278–289.

112 P. Clauwaert, K. Rabaey, P. Aelterman, L. D. Schamphelaire, T. H. Pham, P. Boeckx, N. Boon and W. Verstraete, *Environ. Sci. Technol.*, 2007, **41**, 3354–3360.

113 A. D. Fonseca, J. G. Crespo, J. S. Almeida and M. A. Reis, *Environ. Sci. Technol.*, 2000, **34**, 1557–1562.

114 R. Epsztein, O. Nir, O. Lahav and M. Green, *Chem. Eng. J.*, 2015, **279**, 372–378.

115 N. Barrabés and J. Sá, *Appl. Catal., B*, 2011, **104**, 1–5.

116 Y. H. Liou, S. L. Lo, C. J. Lin, C. Y. Hu, W. H. Kuan and S. C. Weng, *Environ. Sci. Technol.*, 2005, **39**, 9643–9648.

117 F. Yao, Q. Yang, Y. Zhong, X. Shu, F. Chen, J. Sun, Y. Ma, Z. Fu, D. Wang and X. Li, *Water Res.*, 2019, **157**, 191–200.

118 H. Xu, J. Wu, W. Luo, Q. Li, W. Zhang and J. Yang, *Small*, 2020, **16**, 2001775.

119 C. Chen, K. Li, C. Li, T. Sun and J. Jia, *Environ. Sci. Technol.*, 2019, **53**, 13868–13877.

120 Q. Hu, Y. Qin, X. Wang, Z. Wang, X. Huang, H. Zheng, K. Gao, H. Yang, P. Zhang, M. Shao and C. He, *Energy Environ. Sci.*, 2021, **14**, 4989–4997.

121 Y. Wang, C. Wang, M. Li, Y. Yu and B. Zhang, *Chem. Soc. Rev.*, 2021, **50**, 6720–6733.

122 M. T. de Groot and M. T. M. Koper, *J. Electroanal. Chem.*, 2004, **562**, 81–94.

123 K. J. Vetter, *Z. Elektrochem.*, 1959, **63**, 1189–1191.

124 G. Schmid, *Z. Elektrochem.*, 1961, **65**, 531–534.

125 X. Zhang, Y. Wang, C. Liu, Y. Yu, S. Lu and B. Zhang, *Chem. Eng. J.*, 2021, **403**, 126269.

126 H. Shin, S. Jung, S. Bae, W. Lee and H. Kim, *Environ. Sci. Technol.*, 2014, **48**, 12768–12774.

127 P. Li, Z. Jin, Z. Fang and G. Yu, *Energy Environ. Sci.*, 2021, **14**, 3522–3531.

128 G.-F. Chen, Y. Yuan, H. Jiang, S.-Y. Ren, L.-X. Ding, L. Ma, T. Wu, J. Lu and H. Wang, *Nat. Energy*, 2020, **5**, 605–613.

129 E. Pérez-Gallent, M. C. Figueiredo, I. Katsounaros and M. T. M. Koper, *Electrochim. Acta*, 2017, **227**, 77–84.

130 H. Niu, Z. Zhang, X. Wang, X. Wan, C. Shao and Y. Guo, *Adv. Funct. Mater.*, 2020, **31**, 2008533.

131 Z. Y. Wu, M. Karamad, X. Yong, Q. Huang, D. A. Cullen, P. Zhu, C. Xia, Q. Xiao, M. Shakouri, F. Y. Chen, J. Y. T. Kim, Y. Xia, K. Heck, Y. Hu, M. S. Wong, Q. Li, I. Gates, S. Siahrostami and H. Wang, *Nat. Commun.*, 2021, **12**, 2870.

132 W. Teng, J. Fan and W. X. Zhang, *ACS Appl. Mater. Interfaces*, 2020, **12**, 28091–28099.

133 J. Li, M. Li, N. An, S. Zhang, Q. Song, Y. Yang and X. Liu, *Proc. Natl. Acad. Sci. U. S. A.*, 2021, **118**, e2105628118.

134 T. Zhu, Q. Chen, P. Liao, W. Duan, S. Liang, Z. Yan and C. Feng, *Small*, 2020, **16**, e2004526.

135 J. Liu, Y. Cai, R. Song, S. Ding, Z. Lyu, Y.-C. Chang, H. Tian, X. Zhang, D. Du, W. Zhu, Y. Zhou and Y. Lin, *Mater. Today*, 2021, **48**, 95–114.

136 R. Sun, Y. Liao, S.-T. Bai, M. Zheng, C. Zhou, T. Zhang and B. F. Sels, *Energy Environ. Sci.*, 2021, **14**, 1247–1285.

137 Y. Pan, R. Lin, Y. Chen, S. Liu, W. Zhu, X. Cao, W. Chen, K. Wu, W.-C. Cheong, Y. Wang, L. Zheng, J. Luo, Y. Lin, Y. Liu, C. Liu, J. Li, Q. Lu, X. Chen, D. Wang, Q. Peng, C. Chen and Y. Li, *J. Am. Chem. Soc.*, 2018, **140**, 4218–4221.

138 H. Shang, T. Wang, J. Pei, Z. Jiang, D. Zhou, Y. Wang, H. Li, J. Dong, Z. Zhuang, W. Chen, D. Wang, J. Zhang and Y. Li, *Angew. Chem., Int. Ed.*, 2020, **59**, 22465–22469.

139 L. Han, S. Song, M. Liu, S. Yao, Z. Liang, H. Cheng, Z. Ren, W. Liu, R. Lin, G. Qi, X. Liu, Q. Wu, J. Luo and H. L. Xin, *J. Am. Chem. Soc.*, 2020, **142**, 12563–12567.

140 A. Guan, Z. Chen, Y. Quan, C. Peng, Z. Wang, T.-K. Sham, C. Yang, Y. Ji, L. Qian, X. Xu and G. Zheng, *ACS Energy Lett.*, 2020, **5**, 1044–1053.

141 D. Gao, T. Liu, G. Wang and X. Bao, *ACS Energy Lett.*, 2021, **6**, 713–727.

142 Y. Wang, Y. Liu, W. Liu, J. Wu, Q. Li, Q. Feng, Z. Chen, X. Xiong, D. Wang and Y. Lei, *Energy Environ. Sci.*, 2020, **13**, 4609–4624.

143 F. Franco, C. Rettenmaier, H. S. Jeon and B. Roldan Cuenya, *Chem. Soc. Rev.*, 2020, **49**, 6884–6946.

144 M. Li, H. Wang, W. Luo, P. C. Sherrell, J. Chen and J. Yang, *Adv. Mater.*, 2020, **32**, 2001848.

145 R. Lang, X. Du, Y. Huang, X. Jiang, Q. Zhang, Y. Guo, K. Liu, B. Qiao, A. Wang and T. Zhang, *Chem. Rev.*, 2020, **120**, 11986–12043.

146 J. Jones, H. Xiong, A. T. DeLaRiva, E. J. Peterson, H. Pham, S. R. Challa, G. Qi, S. Oh, M. H. Wiebenga,

X. I. P. Hernández, Y. Wang and A. K. Datye, *Science*, 2016, **353**, 150–154.

147 J. Gu, M. Jian, L. Huang, Z. Sun, A. Li, Y. Pan, J. Yang, W. Wen, W. Zhou, Y. Lin, H. J. Wang, X. Liu, L. Wang, X. Shi, X. Huang, L. Cao, S. Chen, X. Zheng, H. Pan, J. Zhu, S. Wei, W. X. Li and J. Lu, *Nat. Nanotechnol.*, 2021, **16**, 1141–1149.

148 C. Paolucci, I. Khurana, A. A. Parekh, S. Li, A. J. Shih, H. Li, J. R. Di Iorio, J. D. Albarracin-Caballero, A. Yezerets, J. T. Miller, W. N. Delgass, F. H. Ribeiro, W. F. Schneider and R. Gounder, *Science*, 2017, **357**, 898–903.

This journal is © The Royal Society of Chemistry 2022

J. Mater. Chem. A, 2022, **10**, 5743–5757 | **5757**